Reduced graphene oxide as the electron transport layer in perovskite solar cell: effect on the photovoltaic performance

O. A. Oyekanmi[a,c], S. Amole[a], O. Akinrinola[a], O. Adedokun[a,b,*], A. K. Dauda[d], F. A. Ojeniyi[a], A. O. Awodugba[a]

[a]*Department of Pure and Applied Physics, Ladoke Akintola University of Technology, P.M.B 4000, Ogbomoso, Nigeria*
[b]*Nanotechnology Research Group (NANO+), Ladoke Akintola University of Technology, Ogbomoso, Nigeria*
[c]*Department of Physical Science, Niger State Polytechnic, P.M.B 001, Zungeru, Nigeria*
[d]*National Agency for Science and Engineering Infrastructure (NASENI), P.M.B 391, Abuja, FCT Nigeria*

ARTICLE INFO

ABSTRACT

Perovskite solar cells (PSCs) have experienced an unprecedented advancement in the last decade owing to their astonishingly attractive properties, especially high-power conversion efficiency (PCE). In this study, the influence of reduced graphene oxide (rGO) on the photovoltaic performance of perovskite solar cells prepared via solution processes-based spin coating method was investigated. X-ray Diffraction (XRD), Fourier Transform Infrared spectrometer (FTIR), UV-visible spectrophotometry, Scanning Electron Microscopy (SEM) were used to study the properties of the prepared films. ITO/MAPbBr$_3$/Gr and ITO/rGO/MAPbBr$_3$/Gr planar PSCs were fabricated via spin coating method. ITO/rGO /MAPbBr$_3$/Gr film achieved a power conversion efficiency (PCE) of 4.1 short circuit current (Jsc) of 7.5 mAcm^{-2} and fill factor (FF) of 61.2% compared to a PCE of 3.6%, Jsc of 6.6 mAcm^{-2} and FF of 58.0% achieved by ITO/MAPbBr$_3$/Gr film. The PSC demonstrated the percentage enhancement value of 16.80% when modified with rGO. This study shows that rGO generated functional groups that act as conducting bridge in reducing the contact resistance between interface of the device.

1. INTRODUCTION

Organic-inorganic methylammonium lead trihalide perovskite is a potential candidate for future commercialization owing to its surpassing properties such as two-dimensional electrical conductivities, ambipolar behaviour, narrow bandgap, long charge carrier diffusion length and favorable charge-transport properties. Nonetheless, photocurrent hysteresis is the major challenge to future commercialization of PSCs. The photocurrent hysteresis set up in perovskite when dangling bonds and vacancies are formed at the grains boundaries (GBs) and the interfaces of the material due to crystallization at low temperatures [1]. Dangling bonds are vehicle for the migration of ionic and molecular species, and also act as charge recombination centres, leading to recombination, hindering charge mobility and extraction, decreasing photovoltaic performance [2].

As a result of this, many attempts have been made to passivate GBs and interfaces defects to improve the efficiency of PSCs [3]. Several studies have shown that self-passivation using excess

---

*Corresponding author Tel. No: +234-703-1195-750.
e-mail:* oadedokun@lautech.edu.ng (O. Adedokun)

PbI_2 and CH_3NH_3I reduced recombination loss at GBs [4]. Other studies showed that excess PbI_2 are detrimental to the overall PCE [5]. Many other passivation media/agents have been developed to maximize the device performance. Organic Lewis acids and bases such as buckminsterfullerene (C_{60}) [6] have drastically reduced the recombination centres in perovskite films leading to increased enhancement in photovoltaic performance. Nevertheless, these self-passivation methods are liable to the preparation conditions, resulting in difficulties associated with reproducibility [3].

Graphene was incorporated at the electron-transport layer (ETL) of PSCs in attempts to passivate dangling bonds and vacancies formed at the GBs of the perovskite films. For instance, Kim *et al* studied the performance evaluation of grapheme oxide incorporated at the ETL in a planar PSC, and recorded a PCE of 3.8% [4]. Wang *et al*. demonstrated a PCE of 4.0% by incorporated graphene at the electron-transport layer (ETL) and coated methylammonium lead iodide ($CH_3NH_3PbI_3$) absorber with poly 3 hexylthiophene/single walled carbon nanotubes (P3HT/SWCNTs) then with poly methyl methacrylate (PMMA) [7]. Samuel *et al* reported a PCE of 4.30% by investigating the photovoltaic performance of graphene oxide incorporated at the ETL in mesoscopic PSC [8].

Additionally, inorganic transition passivation materials such as titanium dioxide (TiO_2) chromium oxide (Cr_2O_4), magnesium manganese oxide (Mg_2MnO_8), manganese oxide (Mn_2O_3), zirconium oxide (ZrO_2) and aluminum oxide (Al_2O_3) have been used to modify the photovoltaic performance of PSCs, owing to their tailored functionalities such as proven wide energy bandgap, astonishing structural modularity, straightforward application methods and versatile passivation influences [9].

Thus, rGO was used mainly because of its wide bandgap, high work function, high electron mobility, high electrical conductivity and completely astonishing structural modularity [10]. It is therefore imperative to investigate the photovoltaic performance of rGO incorporated at the ETL of the planar PSCs. In the research, rGO synthesized by modified Hummer's method was used to sensitize three dimensional organic-inorganic methylammonium lead tribromide perovskite material for all-solid-state perovskite solar cells, and its influence on the properties and photovoltaic performance of modified PSCs were evaluated.

2. MATERIALS AND METHOD

2.1. MATERIALS

Lead (II) bromide ($PbBr_2$) 98% purity, methylammonium bromide (CH_3NH_3Br) 98% purity, graphite, potassium permanganate ($KMnO_4$) 96% purity, dimethyl formamide (DMF) 97% purity, isopropanol ($CH_3CH(OH)CH_3$) 99% purity, ethanol (CH_3CH_2OH) 99% purity, hydrochloric acid (HCl) 97% purity, hydrogen tetraoxosulphate (VI) acid (H_2SO_4) 97% purity, indium doped tin oxide (ITO) glass and detergent were purchased from commercial suppliers (Sigma-Aldrich). Lead (II) bromide and methylammonium bromide were used as precursors, and dimethyl formamide was used as solvent.
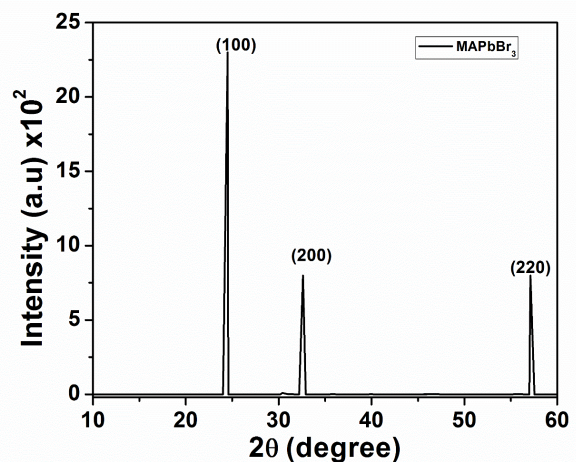
2.2. METHOD

Figure 1. XRD pattern of MAPbBr$_3$ nanoparticles film.

2.2.1. Synthesis and deposition of methyl ammonium lead tribromide (MAPbBr$_3$) solution

Lead (II) bromide ($PbBr_2$) and of methyl ammonium bromide (MABr) solutions were synthesized via solution process-based method. First, lead (II) bromide ($PbBr_2$) was preheated for 10 minutes at 100 ^{o}C to evaporate possible humidity within. In a process to synthesize 1 M of methylammonium lead tribromide (MAPbBr$_3$) solution, 371 mg of lead (II) bromide ($PbBr_2$) and 112 mg of methylammonium bromide (MABr) were mixed with 1 mL of dimethyl formamide (DMF) in a test tube and heated 250 ^{o}C. This temperature was chosen in order to dissolve $PbBr_2$ in DMF. The solution was stirred vigorously to prevent crystallization of $PbBr_2$ [6]. The synthesized was then spin coated on ITO glass slide at 2000 rpm for 30 s, and annealed at 100 ^{o}C for 20 minutes to improve its functionality. Equation 1 represents the reaction equation for the synthesis of methylammonium lead tribromide [11].

$$MABr + PbBr_2 \rightarrow MAPbBr_3. \tag{1}$$
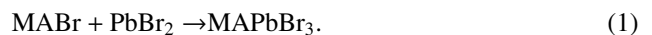
2.2.2. Synthesis and deposition of reduced graphene oxide (rGO) solution

The procedure was adapted from literature review [12]. At first, the mixture of 5g of graphite and 15g of potassium per manganese was added slowly to 400mL of hydrogen tetraoxosulphate (VI) acid solution in a three neck flask and stirred vigorously at 50 ^{o}C for 2 hours. After complete mixing of the solution, 3mL of hydrogen peroxide and 400g of ice was added to the solution to stop the reaction. After that, 200mL of distilled water was added for pH neutralization. The solution was the washed with 200mL of HCl to remove metal ions and other impurities. Ultimately, 200mL of ethanol was added to drying the resultant reduced graphene oxide [12]. 1.00 M of rGO was prepared in ethanol, and spin-coated on ITO glass slide at 2000 rpm for 30 s. The film was then annealed at 100°C for 1 hr.

Table 1. Lattice parameters of MAPbBr$_3$ halide perovkite film.

Peak	2θ (°)	FWHM	Intensity (a.u)	$\sin\theta$	$\cos\theta$	d (Å)	hkl	L (nm)
1	24.5	1.022	2300	0.2449	0.9743	7.258	100	8.31
2	45.4	1.122	800	0.2773	0.9607	3.991	200	8.02
3	47.1	1.135	800	0.3842	0.9232	3.854	220	7.98
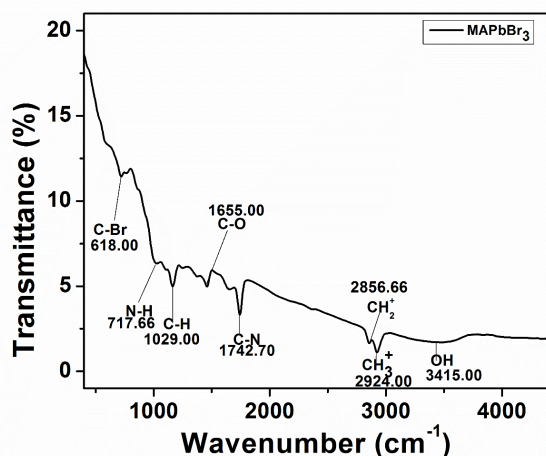
Figure 2. FTIR spectra of MAPbBr$_3$ film.

2.3. DEVICE FABRICATION

Glass/ITO /rGO/ MAPbBr$_3$/ Graphite and Glass/ITO / MAPbBr$_3$/ Graphite photoanodes were fabricated by spin-coating method. In order to fabricate Glass/ITO /rGO/ MAPbBr$_3$/ Graphite, one layer of synthesized methylammonium lead tribromide solution was spin-coated at 2000 rpm for 30 s. The fabricated methylammonium lead tribromide was dried thermally at 100 C for 1 hr. Afterward one layer of a solution of 0.006g graphite in 0.04g of ethanol was spin-coated at 2000 rpm for 30 s. The fabricated film was then dried thermally at 100 ^{o}C in an oven. In a bid to fabricate Glass/ITO /rGO/ MAPbBr$_3$/ Graphite photoanode, 1.00 M of rGO was prepared in ethanol. One layer of rGO solution was spin-coated at 2000 rpm for 30 s on a cleaned ITO glass slide, and annealed at 80 ^{o}C for 1 hr. One layer of synthesized methylammonium lead tribromide solution was spin-coated at 2000 rpm for 30 s. The CH$_3$NH$_3$I$_3$ was dried thermally at 100 C for 1 hr to avoid agglomeration. Afterward one layer of a solution of 0.006g graphite in 0.04g of ethanol was spin-coated at 2000 rpm for 30 s. The fabricated film was then dried thermally at 100 ^{o}C in an oven to prevent agglomeration [8].

2.4. CHARACTERIZATION AND MEASUREMENT

X-ray diffraction pattern was obtained with the Rigaku D/Max-lllC X-ray diffractometer developed by the Rigaku Int. Corp. Tokyo, Japan and set to produce diffractions at scanning rate of 2 ^{o}/min in the 2 to 50° at room temperature with a Kα radiation set at 40kV and 20mA for the MAPbBr$_3$/rGO/ITO/MAPbBr$_3$/Gr and ITO/rGO/MAPbBr$_3$/Gr photoanode films. Fourier transform infrared spectroscopy (FTIR) analysis was performed in all samples using Pelkin Elmer 3000 MX spectrometer to investigate

the nature of bonds and the quality of films. All spectra were recorded from 4000 to 400 cm^{-1}. The ultraviolet-visible spectrophotometer (Lambda 950) was used to study the optical properties such as transmittance, absorbance, and wavelength of the absorption spectra. Scanning electron microscopy (SEM) images was acquired using a JEOL 6010LV microscope at an accelerating voltage of 15 kV and a working distance of 11 mm. SEM was used to observe and analyzed the surface morphologies of the solid-state perovskite thin film. The current-voltage (I-V) measurement of the formed cells were carried out under AM 1.5G (100 mWcm^{-2}) solar illumination.

2.5. THEORETICAL CONSIDERATION

The band gap of perovskite film is calculated by Tauc's plot which is expressed as [13]:

$$(\alpha h v)^2 = (hv - E_g), \tag{2}$$

$$\alpha = \frac{A}{d}. \tag{3}$$

For the determination of interplanar distance Bragg's law was used

$$n\lambda = 2d\sin\theta. \tag{4}$$

Here θ is the one half of peak diffraction angle or Bragg's angle, d is the interplanar distance, λ represents the Kα wavelength, which in our case is 1.5418 A and n is the mode of vibration.

The crystallite size (L) was determined from the Scherrer equation [14]:

$$L = \frac{K\lambda}{\beta\cos\theta}, \tag{5}$$

where K is the Scherrer constant (0.9), λ is the wavelength and β is the full width (in radians) of the peak at the half maximum (FWHM) intensity and λ is the one half of peak diffraction angle or Bragg's angle.

Lattice stain (ε) of the materials was calculated by the relation [15]:

$$\varepsilon = \frac{\beta\cos\theta}{4}, \tag{6}$$

θ is the one half of peak diffraction angle or Bragg's angle and ε is the lattice strain [16].

The dislocation density δ was calculated using the relation

$$\delta = \frac{1}{L^2}, \tag{7}$$

where δ is the dislocation density and L is the crystallite size.

To measure the efficiency of a solar cell, the current density of a device is obtained as a function of applied voltage. Such
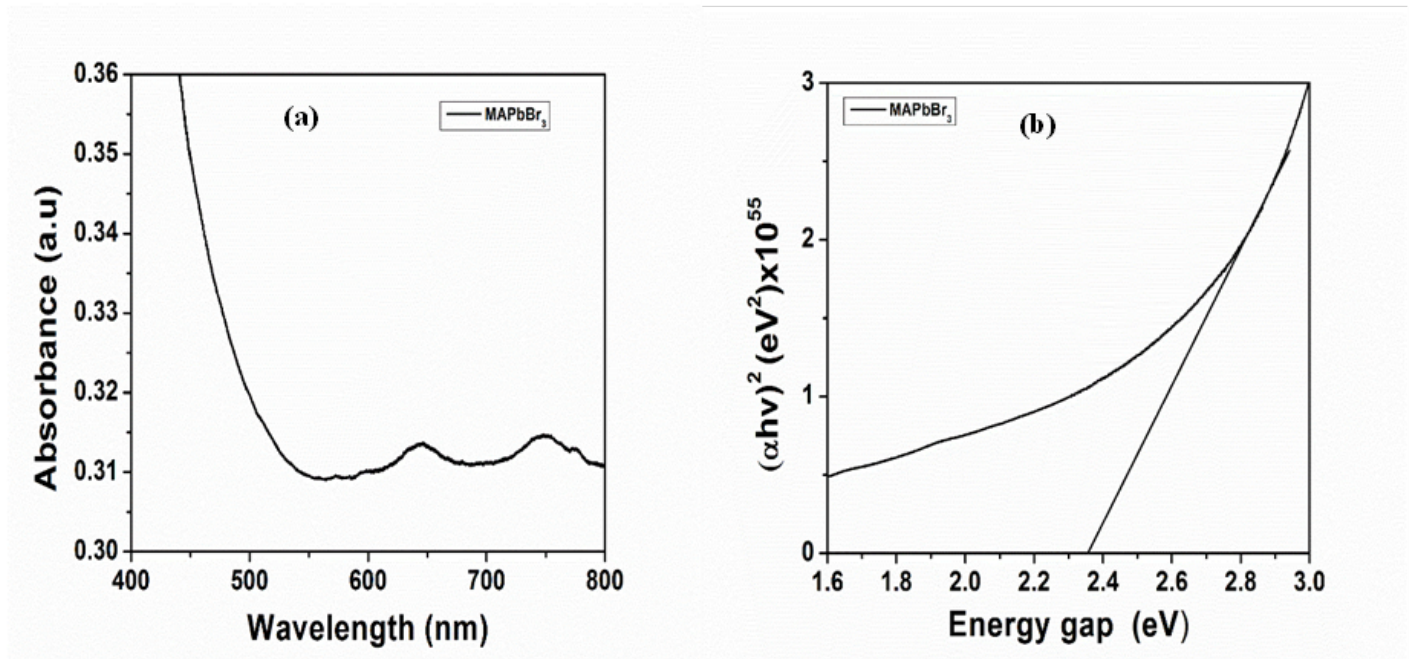
Figure 3. Absorbance-wavelength plots (b) $(\alpha h v)^2$-Eg plots of MAPbBr$_3$ thin film.
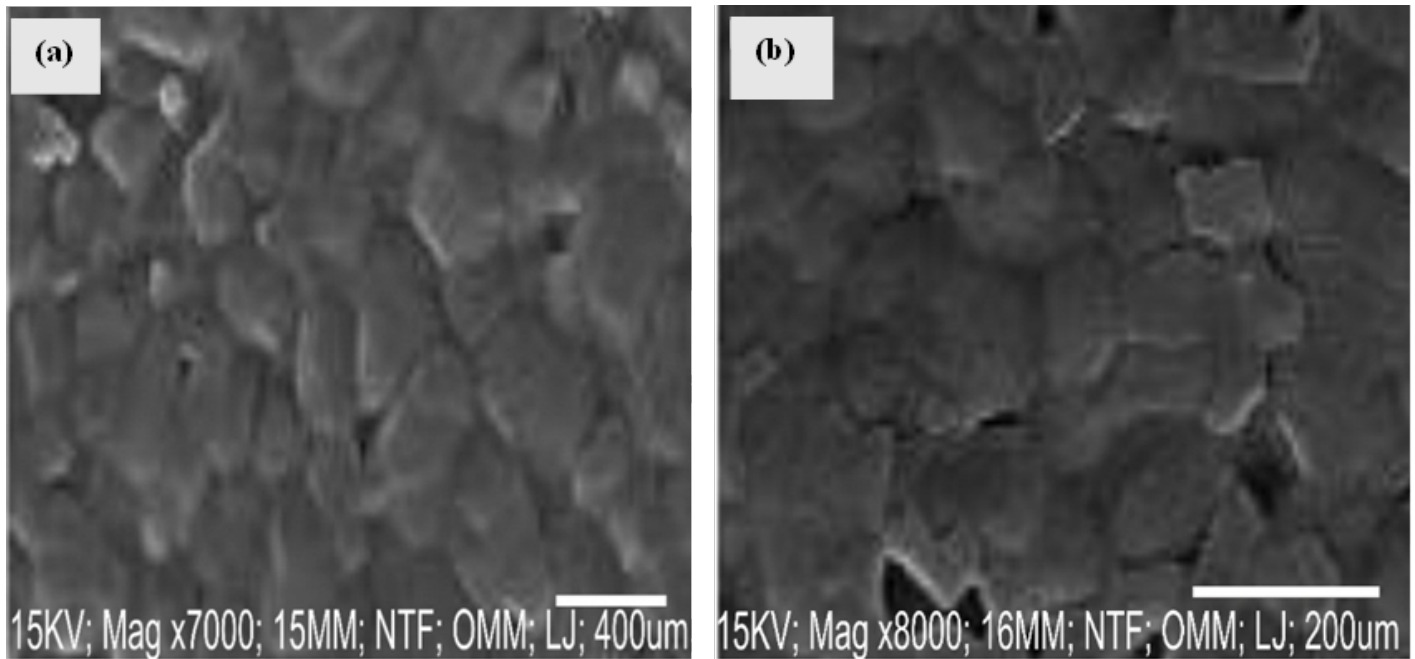

Figure 4. SEM images of MAPbBr$_3$ film.

Table 2. Structural parameters of rGO film.

2θ (°)	FWHM (°)	Count (a.u)	d (Å)	hkl	L (nm)	ε (%)	δ (nm^{-2})
22.1	0.181	550	4.881	100	46.44	0.044	0.000463
28.8	0.121	900	3.309	310	70.83	0.029	0.000199

a curve provides the parameters required to calculate efficiency [17].

$$\eta = \frac{p_{out}}{p_{in}} = \frac{J_{sc}V_{OC}FF}{p_{in}}, \tag{8}$$

where η is efficiency, P_{out} is the output power of a device, P_{in} the input power of the incident light, J_{sc} is the short-circuit current density.
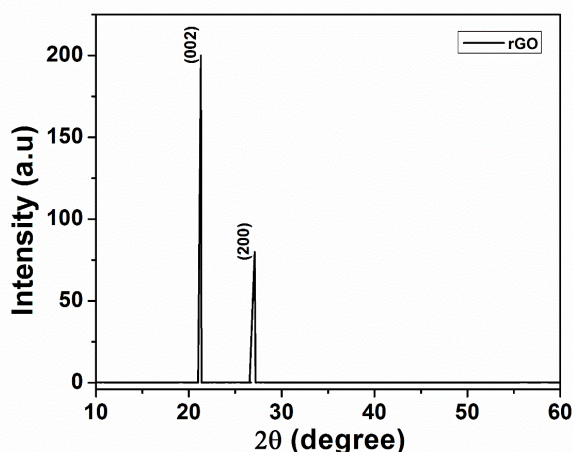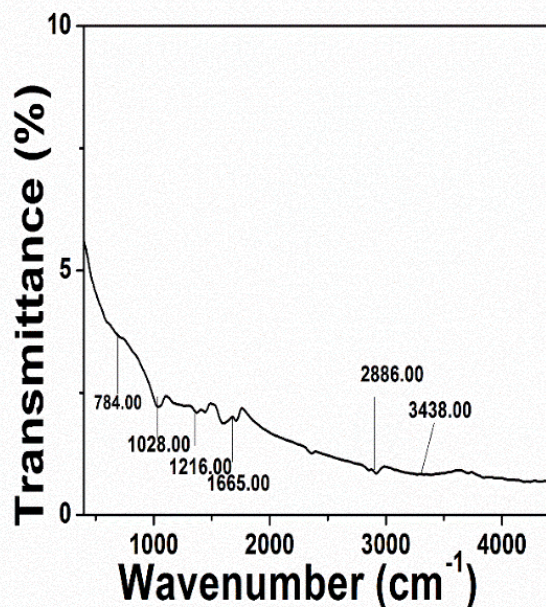
Figure 5. XRD pattern of rGO film.

Figure 6. FTIR spectrum of rGO thin film.

Fill factor (FF) is calculated by the relation [18] :

$$FF = \frac{J_{mp}V_{mp}}{J_{sc}V_{oc}},\qquad(9)$$

where V_{oc} is the open-circuit voltage, J_{mp}, and V_{mp} are the current density and voltage of the device at its maximum power point, where the value of $J \times V$ is at its maximum in the JV curve.

3. RESULTS AND DISCUSSION

3.1. STUDY OF CHARACTERISTICS OF SYNTHESIZED MAPBBR₃ FILM

3.1.1. XRD characterization of MAPbBr₃ halide perovskite film

The XRD pattern of the synthesized MAPbBr₃ halide perovskite is shown in Figure 1. All the peaks were well-indexed and matched with the cubic phase of MAPbBr₃ halide perovskite, corresponding to JCPDS card number 42-1411. In addition, the broadness and intensity of the peaks of the XRD reflections indicates the smaller size of the formed nanoparticles. From Table 1, the mean size of the crystallites was calculated to be 8.1 nm using Scherrer equation. The most prominent perovskite peak is at the (100) reflection, observed at $2\theta = 24.5^o$ compatible with a single-crystalline phase, and strongly indicative of formation of high quality MAPbBr₃ films. Three other strong diffraction peaks are located at 24.5, 45.4^o and 47.1^o corresponding to the (100), (200) and (220) planes respectively and other low peaks at 10° and 32.6^o assigned to (002) and (101) respectively, which confirm the formation of a cubic perovskite structure. Additionally, the absence of peaks at 9°, 19° and 29° indicates absence of MAI crystallization in perovskite films, supporting the conversion of the precursor materials into MAPbBr₃ films [19].

3.1.2. FTIR characterization of *MAPbBr₃ film*

Figure 2 presents FTIR spectra of MAPbBr₃ halide perovskite thin film. The peak at 3415.00 cm^{-1} with additional presence of spectra at frequencies of 1655.00, 1459.28, 1376.17, 1251.00, 1163.24, 1029.00 and 765,00 cm^{-1} confirms the existence of hydroxyl (- OH). And again, the peak at 1742.70 cm^{-1} is characteristic of the C=N stretching mode of methyl ammonium (MA) cation, and the sharp peaks at 2924.00, 2856.66, 1459.28 and 721.00 cm^{-1} are characteristics of the linear aliphatic compound. The presence of peak at 1029.00 cm^{-1} also confirmed the vibration of N-H stretches of MA cation. Moreover, the appearance of spectra at 1251.00, 1163.00, 1259.00, 765.00 and 721.00 cm^{-1} suggest C-C vibrations. The appearances of peaks at 2924.00 and 2856.66 cm^{-1} signifying the presence of C-H stretching mode [20].

Furthermore, the band at 3482 cm^{-1} responsible for the labile –OH stretching mode due to surface adsorbed water and the band at 1655.00 cm^{-1} is attributed to C-O stretching mode corresponding to the surface of MAPbBr₃. In the fingerprint region of the FTIR spectrum of MAPbBr₃ halide perovskite, there are two absorption peaks at 717.66 and 618.00 cm^{-1}, which can be assigned to aromatic CH out-of-plane bend and presence of the C-Br stretching mode. Several molecular vibration frequencies are identified which include N-H (Vc-o,1029.00 cm^{-1}), C=N ($V_{C=N}$, 1742.70 cm^{-1}), C-C ($V_{C=C}$, 1259.00 cm^{-1}), C-H (V_{C-H}, 2856.66 cm^{-1}), C-Br (V_{C-Br}, 618.00 cm^{-1}) and O-H (V_{C-OH},3415.00 cm^{-1}). These functional groups are in keeping with cubic phase of MAPbBr₃ halide perovskite [20].

3.1.3. Optical characterization of synthesized MAPbBr₃ film

Figure 3 shows absorbance-wavelength plot of MAPbBr₃ film with its distinct absorption edges. It is clear that the absorption onset systemically located at 530 nm, 656 nm, 746 nm, and 782 nm. This shows that MAPbBr₃ film absorbs within the visible region with longer wavelength range of between 395-800 nm. The graph also shows that the perovskite material has a higher absorption coefficient within the visible region of the solar spectrum [21]. Hence, it has satisfied the major requirement to be used as a light harvester in this research. The absorption onset was used to calculate the bandgap in Figure 3b using Tauc's plot. The bandgap of the synthesized MAPbBr₃ film is 2.4 eV. The
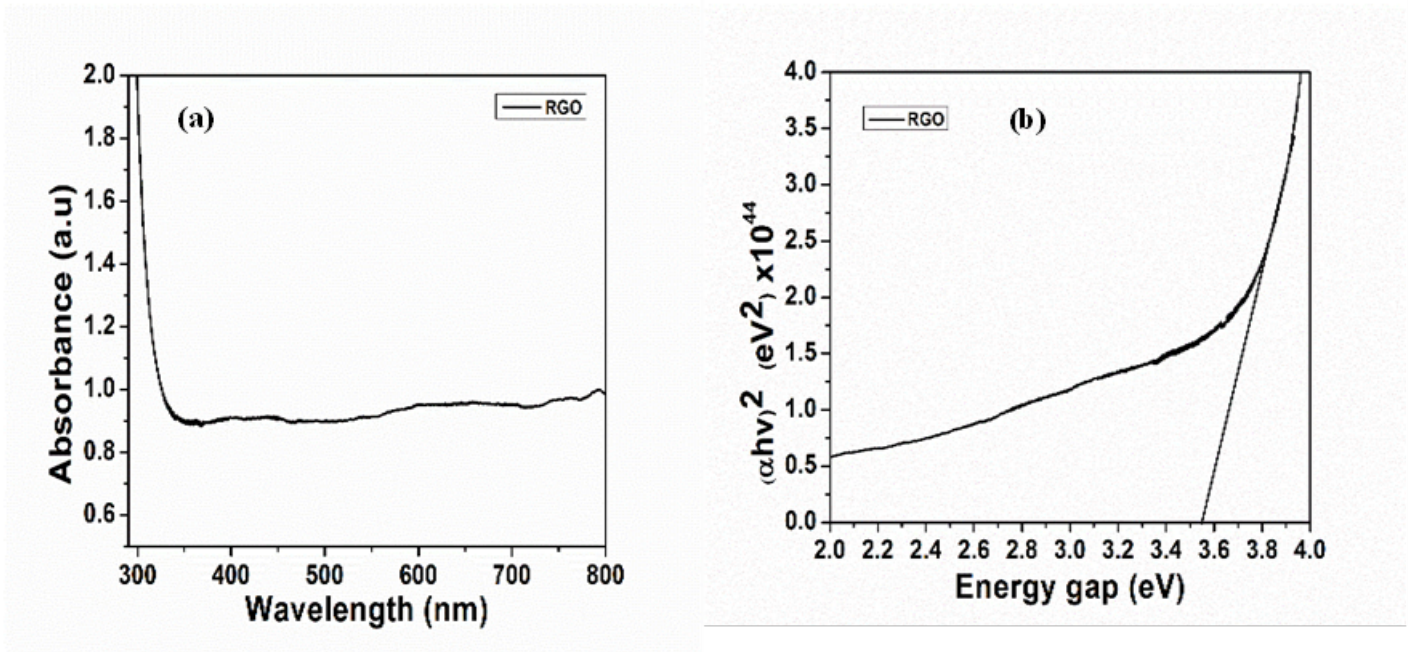
Figure 7. (a) Absorbance-wavelength plot (b) $(\alpha h v)^2$-Eg plots of rGO film.
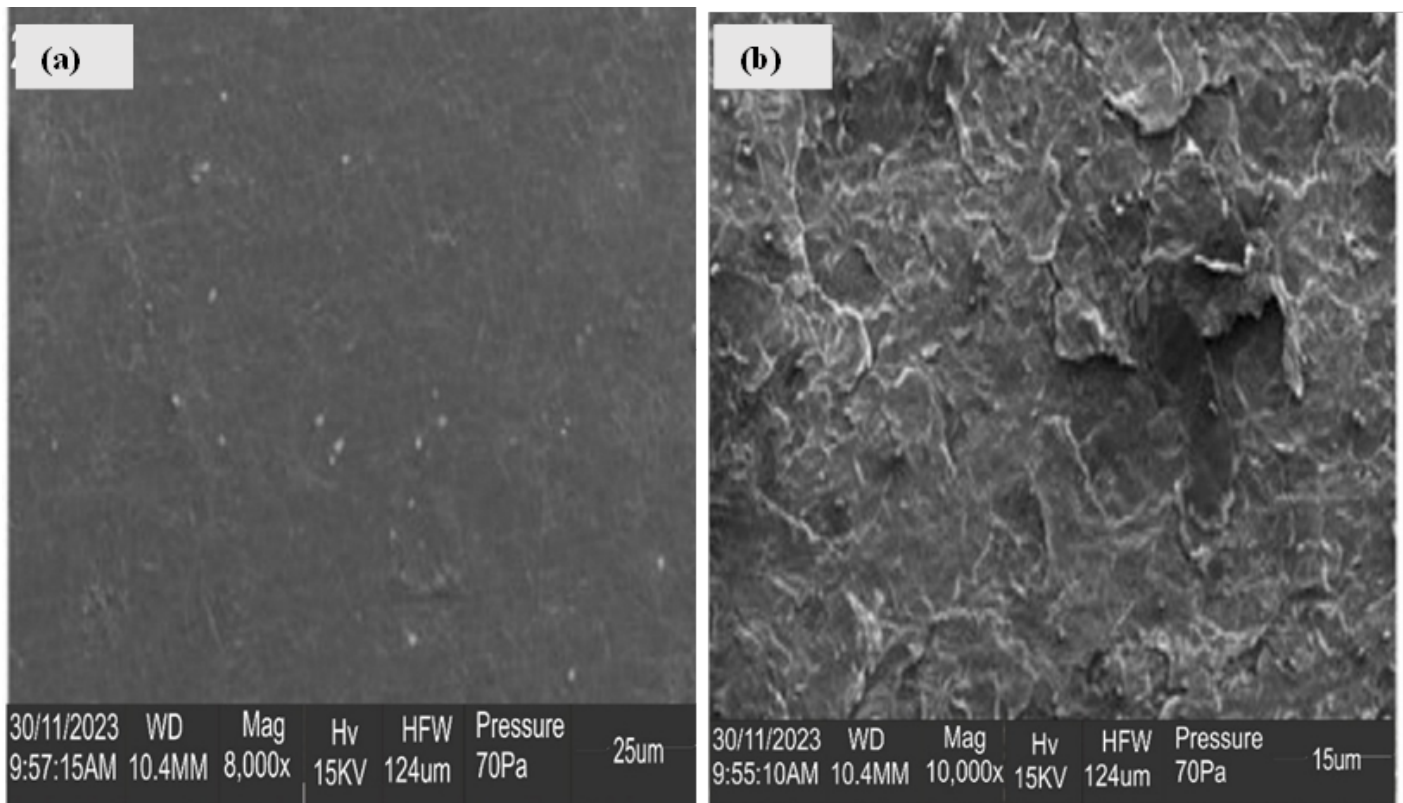

Figure 8. SEM images of rGO film.

bandgap value of 2.4 eV for perovskite is within the acceptable range 2.3 - 2.6 eV [22].

3.1.4. SEM characterization of MAPbBr$_3$ film

Figure 4 shows the SEM image of MAPbBr$_3$ halide perovskite films at the magnifications of 7000 and 8000. The SEM im-
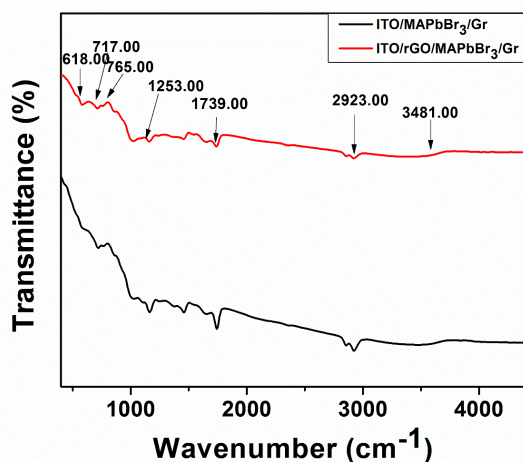
ages demonstrate high film coverage and uniform morphology with apparent crystallites typical of MAPbBr$_3$ halide perovskite films. Individual perovskite crystallites were elongated and well-defined. There is evidence of rounding at the edges of the crystallites and no cracks were observed, indicating tremendous adherence and improved morphology [23]. The average grain size was

Table 3. Lattice parameters comparison of ITO/MAPbBr$_3$/Gr and ITO/ rGO /MAPbBr$_3$/Gr halide perovkite devices.

Glass/ITO/MAPbBr$_3$/G				Glass/ITO/rGO/MAPbBr$_3$/Gr			
2θ (degree)	FWHM	d (Å)	L (nm)	2θ (degree)	FWHM	d (Å)	L (nm)
26.0	0.212	3.422	40.18	26.5	0.212	3.359	40.22
32.2	0.122	2.776	70.82	32.6	0.120	2.743	72.07
45.2	0.135	2.003	66.60	45.6	0.112	1.987	80.40
55.0	0.142	1.667	65.91	55.1	0.129	1.664	72.58

Table 4. Photovoltaic performance comparison of ITO/MAPbBr$_3$/Gr and ITO/rGO/MAPbBr$_3$/Gr halide perovkite devices.

Device	Archetecture	J$_{SC}$ (mAcm^{-2})	V$_{OC}$ (V)	FF (%)	PCE (%)
1	ITO/MAPbBr$_3$/Gr	6.6	0.90	58.0	3.5
2	ITO/rGO/MAPbBr$_3$/Gr	7.5	0.91	61.2	4.1
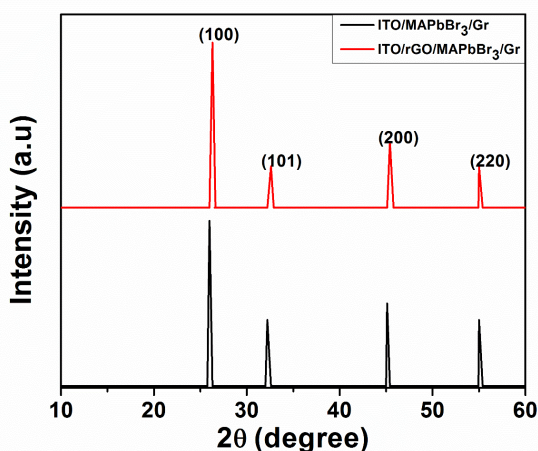
Figure 9. XRD spectra of ITO/MAPbBr$_3$/Gr and ITO/ rGO /MAPbBr$_3$/Gr films.

Figure 10. FTIR spectra of ITO/MAPbBr$_3$/Gr and ITO/rGO/MAPbBr$_3$/Gr Film.

measured to be around 200μm using intercept technique. This result differs from the calculated crystallite size of the synthesized MAPbBr$_3$ halide polycrystalline perovskite film using Scherrer equation owing to agglomeration of the crystallites.

3.2. STUDY OF CHARACTERISTICS OF SYNTHESIZED RGO FILM

3.2.1. XRD characterization of rGO film

The XRD pattern of the synthesized rGO film as shown in Figure 5 demonstrated diffraction peaks at 2θ = 22.10° and 2θ = 28.20° which is the characteristics of carbonaceous material. The most prominent peak located at 2θ = 22.10° corresponding to orientation along (002) basal plane and other strong diffraction peak at 2θ = 22.10° corresponding to orientation along (200) basal planes, which consistent with results obtained for graphene oxide by Mohamed et al, 2015. The (hkl) indexing was performed with reference to JCPDS card number 41-1445. As seen in Table 2, the average d-spacing, lattice strain and crystallite size were calculated to be ~ 3.63Å, 0.0365% and ~ 506 nm using Scherrer equation. The large interlayer spacing of rGO was due to the existence of oxygenated functional group on *rGO* during the harsh oxidation treatment of graphite powder and also the intercalation of water molecules [11].

3.2.2. FTIR characterization of rGO film

As observed in Figure 6, the hydroxyl compounds functional group (–OH) formed at the peak with a wavenumber of 3438.51 cm^{-1}, the aromatic carbon functional group (C=C) formed at the peak with a wavenumber of 1665.02 cm^{-1}, and the epoxy functional group (–CO) formed at the peak with a wavenumber of 1216.14 cm^{-1}. Additionally, alkoxy functional group(–C–O) is located at the peak with a wavenumber 1028.88 cm^{-1} and the absorption peak with a wavenumber of 2886.00 cm^{-1} signifying the existence –C-H stretching mode [24].

3.2.3. Optical characterization of synthesized rGO film

Figure 7a shows absorbance-wavelength plot of *rGO* with its distinct absorption edge. The characteristic absorbance peak at around 300 nm was observed for the sample, which is consistent with the previous studies [25]. The absorbance peak is due to electronic transition between the molecule having an intermediate ionic degree in conformity with those of the synthesized molecular material. At such wavelength, no visible light can be absorbed since rGO absorbing within the ultra-violet region [25]. The plot shows that *rGO* was not capable of harvesting visible
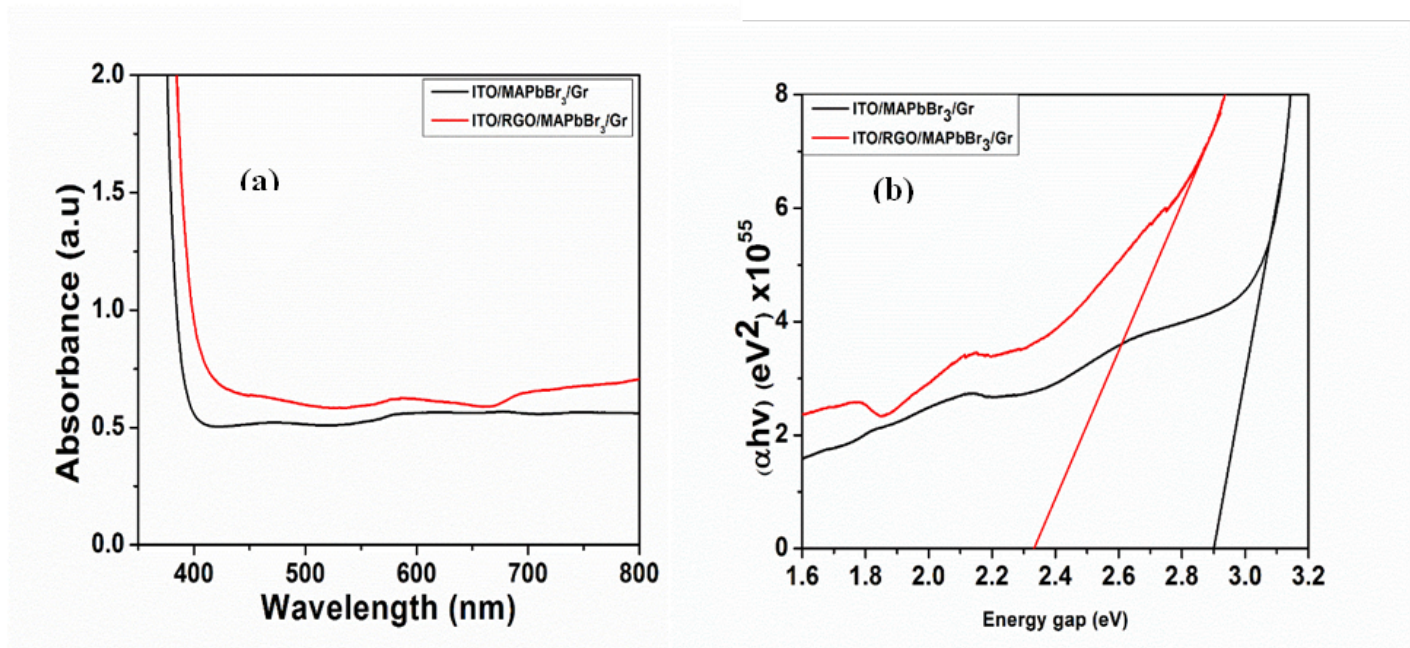
Figure 11. (a) Absorbance-wavelength plot (b) $(\alpha h v)^2$-Eg plots of ITO/MAPbBr$_3$/Gr and ITO/*rGO*/MAPbBr$_3$/Gr film.
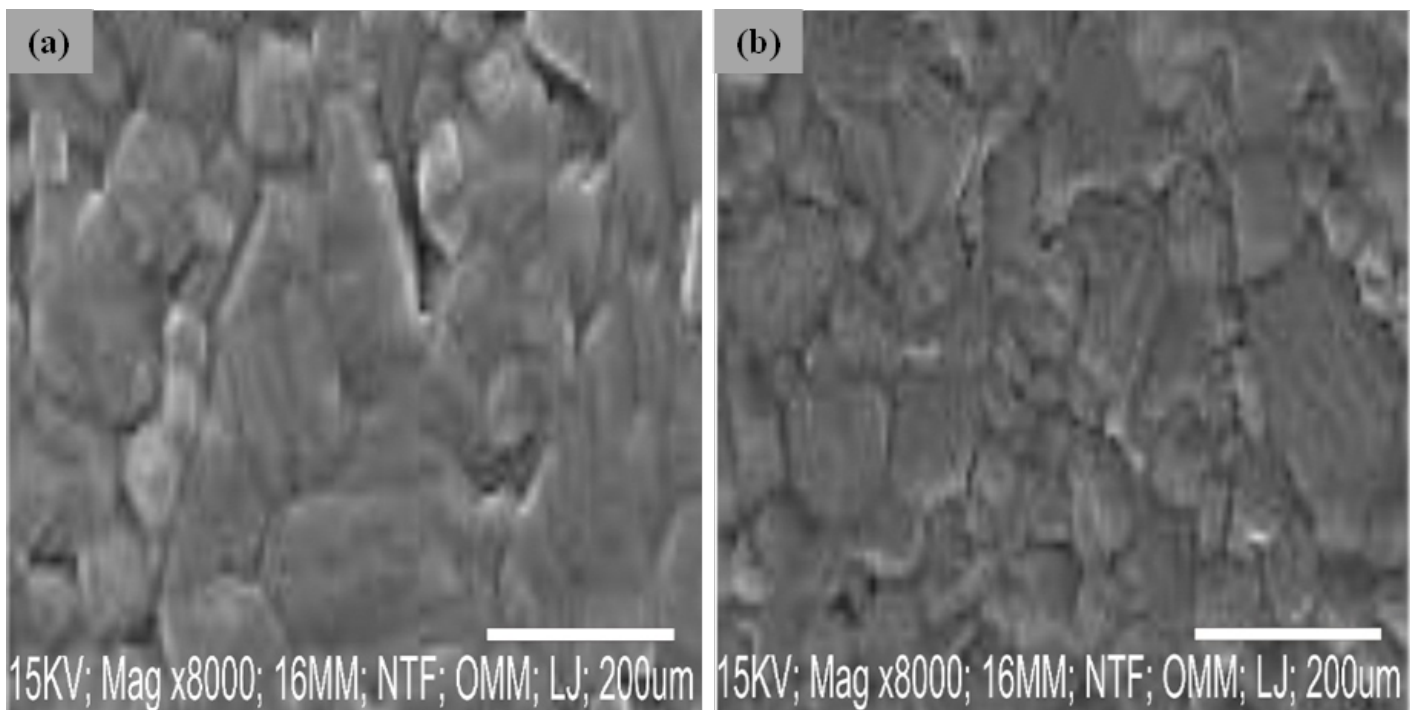

Figure 12. SEM images of ITO/MAPbBr$_3$/Gr and ITO/rGO/MAPbBr$_3$/Gr film.

light within the solar spectrum. The inability of rGO to absorbs light in the longer region of the solar spectrum therefore, clearly indicates that it will not inhibit the transmittance of light to the absorbing layer of the about-to-be-formed solar cell. However, it acts as an insulator because between visible and near infrared region where there is no obvious peak appeared.

The result of band gap energy analysis using the Tauc's plot method for *rGO* is shown in the plot of α^2 against the energy of the photon [13]. As seen in Figure 7b, the extrapolation of the linear part to the energy axis gave the band gap as 3.50 eV for *rGO*, which was probably due to exfoliation of graphite layer allowing easy transfer of electrons. This energy band gap for *rGO* is within the acceptable range of 3.2 -4.0 eV [17].

3.2.4. SEM characterization of rGO film

SEM image of *rGO* at 8000 and 10000 magnifications are shown in Figure 8a-b. The morphology of rGO revealed sheet-like structures which are different in size. The overlapping layers of
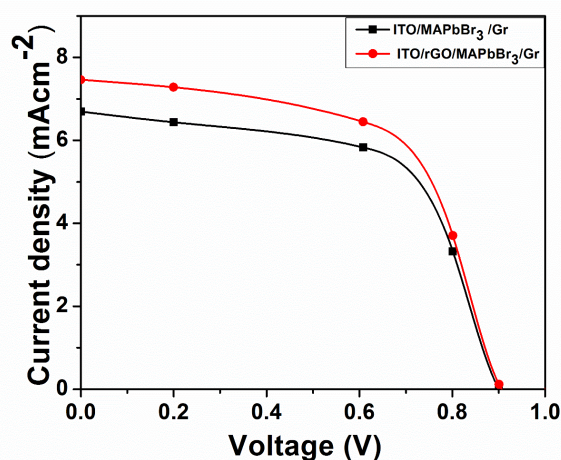
Figure 13. J-V curves of ITO/MAPbBr$_3$/Gr and ITO/rGO/MAPbBr$_3$/Gr film.

flakes with arbitrary shapes are random in-shape orientation [24]. The flakes seemed to aggregate owing to catalytic oxidation of graphite by surphuric acid [26].

3.3. STUDY OF CHARACTERISTICS OF FABRICATED ITO/MAPBBR$_3$/GR AND ITO/RGO/MAPBBR$_3$/GR FILMS

3.3.1. XRD characterization of ITO/MAPbBr$_3$/Gr and ITO/rGO/MAPbBr$_3$/Gr films

Figure 9 shows the diffraction patterns for ITO/MAPbBr$_3$/Gr and ITO/ *rGO* /MAPbBr$_3$/Gr. The highest intensity of diffraction peak is (100), which suggests the cubic phase of the perovskite layer. It is also observed that the intensity of this peak increased which signified that *rGO* has been successfully incorporated into the MAPbBr$_3$ halide perovskite thin film. The most prominent absorption peak (100) has its Bragg angle assigned to 26.8^o. Three other strong peaks (101), (200) and (220) have their Bragg angles corresponding to 34.5, 45.2 and 55.0^o respectively. There was a slight right shifting displacement of the most prominent peak (100) owing to effective incorporation of *rGO* into ITO/MAPbBr$_3$/Gr matrix. As seen in Table 3, the photoanode modified with *rGO* showed improved crystallite size. This result consistent with the inclusion of dopants in to perovskite structure [8].

3.3.2. FTIR characterization of ITO/MAPbBr$_3$/Gr and ITO/rGO/MAPbBr$_3$/Gr film

Figure 10 shows the FTIR spectra of ITO/MAPbBr$_3$/Gr and ITO/ *rGO* /MAPbBr$_3$/Gr photoanodes. As shown in Figure 10, the peak at 1740.85 cm^{-1} in ITO/MAPbBr$_3$/Gr spectra is strongly indicative of C=N stretching mode of methyl ammonium (MA) cation, which has been slightly shifted to 1739.00 cm^{-1} due to *rGO* incorporation in ITO/ *rGO* /MAPbBr$_3$/Gr. Besides, there is an appearance of right shifting displacement in the vibration of N-H stretch of methyl ammonium (MA) cation. Additionally, the prominent shift of spectra from 3415.00 to 3482.00 cm^{-1}, and additional shifting from 1651.00 to 1655.00, 1458.61 to 1459.28, 1158.66 to 1163.24 and 1004.00 to 1029.00 cm^{-1} indicate dipole

interaction of methyl ammonium cation with the components of reduced graphene oxide in the solution. The bands 1315.00 and 2924.47 cm^{-1} are distended and disappearance of a peak at 1239.00 cm^{-1} is largely due to the existence of C-N stretching mode.

In addition, the presence of peaks at 1255.00 cm^{-1} signifying C-C vibration shifted to 1253.00 cm^{-1}, and the band at 618.00 indicating C-Br stretching mode. The sharp band at 1740.85 cm^{-1} is replying the existence of the (simple carbonyl compounds) C=N stretch methyl ammonium (MA) cation since there is no specific peak for aldehyde at between 2700 and 2800 cm^{-1}. In the fingerprint region of the FTIR spectrum of *rGO*/MAPbBr$_3$ halide perovskite thin film, there are two main absorption peaks at 721.00 and 769.00 cm^{-1}, which can be assigned to aromatic CH out-of-plane bend and C-C bonds between rings [27]. These two peaks are similar to those appear in the FTIR spectrum of the *rGO* thin film, which confirms the successful incorporation of *rGO* into ITO/MAPbBr$_3$/Gr halide perovskite thin film.

3.3.3. Optical characterization of synthesized ITO/MAPbBr$_3$/Gr and ITO/rGO/MAPbBr$_3$/Gr films

Figure 11(a) shows absorbance-wavelength plot of ITO/MAPbBr$_3$/Gr and ITO/*rGO*/MAPbBr$_3$/Gr photoanodes with their distinct absorption peaks. The characteristic absorbance peaks were observed at wavelength 455 nm, 582 nm, and 695 nm for ITO/*rGO*/MAPbBr$_3$/Gr photoanode, and at higher absorbance compared to ITO/MAPbBr$_3$/Gr photoanode where peaks were substantially reduced. This is largely due to incorporation of *rGO* into ITO/MAPbBr$_3$/Gr specie, shifting the energy level to a negative potential in a quasi-state and make it absorb photons at longer wavelength up to near infrared region of the solar spectrum [8]. Additionally, there is a red shift in the absorption spectra of ITO/*rGO*/MAPbBr$_3$/Gr, which is a positive shift of the absorbance wavelength towards the red region of the solar spectrum, leading to longer absorbance wavelength and the broadening of the absorption spectra due to a change in the band gap of the material.

The absorption coefficient-energy gap plot of ITO/MAPbBr$_3$/Gr and ITO/*rGO*/MAPbBr$_3$/Gr photoanodes is shown in Figure 11b. The band gap of fabricated ITO/MAPbBr$_3$/Gr solar cell was extrapolated to be 2.86 eV, and that of ITO/*rGO*/MAPbBr$_3$/Gr was grossly reduced to 2.31 eV. Therefore, the reduction of energy gap consequent upon the activation of ITO/MAPbBr$_3$/Gr specie with *rGO* material shifted the energy level to a negative potential in a quasi-state and make it absorb photons at longer wavelength up to near infrared region of the solar spectrum.

3.3.4. SEM characterization of synthesized ITO/MAPbBr$_3$/Gr and ITO/rGO/MAPbBr$_3$/Gr films.

Figure 12 (a) and (b) show the SEM micrographs of fabricated ITO/MAPbBr$_3$/Gr and ITO/rGO/MAPbBr$_3$/Gr photoanodes. The SEM micrograph demonstrated an evidence of high film coverage, high degree of homogeneity, compositional uniformity, and thus the grain boundaries were ubiquitous [9]. No evidence of cracks was observed throughout the surfaces of the photoanodes. It should be noted that ITO/rGO/MAPbBr$_3$/Gr photoanode showed improved smoothness which is highly in-

dicative of enhancement in the crystallinity [28].

3.3.5. Photovoltaic evaluation of synthesized ITO/MAPbBr$_3$/Gr and ITO/rGO/MAPbBr$_3$/Gr films

The performance evaluation of photovoltaic parameters such as Jsc, Voc, FF and PCE were obtained from the J-V curves of ITO/MAPbBr$_3$/Gr and ITO/rGO/MAPbBr$_3$/Gr photoanodes as shown in Figure 13. As seen in Table 4, the inclusion of rGO into the second device produced enhanced values of Jsc from 6.6 mAcm^{-2} to 7.5 mAcm^{-2}, V_{OC} from 0.90 V to 0.91V, FF from 58.0 % to 61.2 % and PCE increased from 3.51% to 4.10%. This is due to the improved charge extraction and transfer ability induced in the second device by introduction of rGO. However, the variation in the values of Voc in both devices could be as a result of hysteresis effect [29]. The percentage enhancement value of 16.80% was realized with rGO modification which promoted grain size enhancement of the perovskite absorber, and improved the crystalline structure of the absorber at the interface between the absorber and the ETL. As the grain size increases, the grain boundary reduces, thereby eliminating the charge trapping regions within the perovskite structure. Furthermore, the centrifugation of rGO reduced its strong agglomeration tendencies due to $\pi - \pi$ stacking interactions [30].

4. CONCLUSION

In this work, ITO/MAPbBr$_3$/Gr and ITO/rGO/MAPbBr$_3$/Gr photoanodes were fabricated using solution process-based spin coating method and their properties were studied. The XRD results of ITO/rGO/MAPbBr$_3$/photoanode showed a variation in diffraction angle corresponding to the crystallographic plane (100), and the FTIR spectra of ITO/MAPbBr$_3$/photoanode modified with rGO showed a slight right shifting displacement in the molecular vibration frequencies indicating enhanced crystallinity. Besides, UV-visible measurements revealed higher characteristic absorbance peaks at wavelength 455 nm, 582 nm and 695 nm for ITO/rGO/MAPbBr$_3$/Gr photoanode. The band gap of fabricated ITO/MAPbBr$_3$/Gr solar cell was extrapolated to be 2.86 eV, and that of ITO/rGO/MAPbBr$_3$/Gr was reduced to 2.31 eV. J-V curve of ITO/MAPbBr$_3$/Gr and ITO/rGO/MAPbBr$_3$/Gr photoanodes showed the PCE increased from 3.51% to 4.10% with a percentage enhancement value of 16.80%. This showed that wide bandgap material with high electron mobility can tune the functionality of perovskite-based solar cells, and shed light on designing of passivation media that further tailor the device's performance.

ACKNOWLEDGMENTS

References

[1] T. H. Han, J. W. Lee, C. Choi, S. Tan, C. Lee, Y. Zhao, Z. Dai, N. D. Marco, S. J. Lee, S. H. Bae, Y. Yuan, H. M. Lee, Y. Huang & Y. Yang, "Perovskite polymer composite cross-linker approach for highly stable and efficient perovskite solar cells", Nature communications **10** (2019) 520. https://www.nature.com/articles/s41467-019-08455-z.

[2] Y. Shao, Z. Xiao, C. Bi, Y. Yuan & J. Huang, "Origin and elimination of photocurrentdent hysteresis by fullerene passivation in CH$_3$NH$_3$PbI$_3$ planar heterojunction solar cells", Nature communications **5** (2014) 5784. https://www.nature.com/articles/ncomms6784.

[3] S. Yang, J. Dai, Z. Yu, Y. Zhou, X. Xiao, X. C. Zeng & J. Huang, "Tailoring passivation molecular structures for extremely small open-circuit voltage loss in perovskite solar cells", Journal of the American Chemical Society **141** (2019) 5781. https://pubs.acs.org/doi/abs/10.1021/jacs.8b13091.

[4] H. Choi, J. Jeong, H. B. Kim, S. Kim, B. Walker, G. H. Kim & J. Y. Kim, "Cesium-doped methylammonium lead iodide perovskite light absorber for hybrid solar cells", Nano Energy **7** (2014) 80. https://www.sciencedirect.com/science/article/abs/pii/S2211285514000731.

[5] G. Tumen-Ulzii, C. Qui, P. Leyden, P. Wang, M. Auffray, T. Fujihara, T. Matsushima, J. W. Lee, S. J. Lee, Y. Yang & C. Aucachi, "Detrimental effect of unreacted PbI$_2$ on the long-term stability of perovskite solar cells", Adv. Mater **32** (2020) 1905035. https://onlinelibrary.wiley.com/doi/abs/10.1002/adma.201905035.

[6] S. Yang, J. Dai, Z. Yu, Y. Zhou, X. Xiao, X. C. Zeng & J. Huang, "Tailoring passivation molecular structures for extremely small open-circuit voltage loss in perovskite solar cells", J. Am. Chem. Soc. **141** (2019) 5781. https://pubs.acs.org/doi/abs/10.1021/jacs.8b13091.

[7] D. Son, J. Lee, X. Y. Choi, I. Jang, S. Lee, P. J. Yoo, H. Shin, N. Ahn, M. Choi, D. Kim & N. Park, "Self-formed grain boundary healing layer for highly efficient CH$_3$NH$_3$PbI$_3$ perovskite solar cells", Nat. Energy **1** (2016) 16081. https://www.nature.com/articles/nenergy201681.

[8] Q. Wang, Q. Dang, T. Li, A. Gruverman & J. Hasung, "Thin insulating tunneling contact for efficient and water-resistant perovskite solar cells", Adv Mater **28** (2024) 6734. https://www.osti.gov/biblio/1342746.

[9] M. U. Samuel, M. Y. Onimisi, J. A. Owolabi, D. Eli & E. O. Mary, "The enhanced photovoltaic performance of perovskite solar cell using carbon nanotubes as hole transport material", The Proceedings of the Nigerian Academy of Science **13** (2020) 148. https://nasjournal.org.ng/site/index.php/pnas/article/view/320.

[10] F. Gao., X. Zhang, Y. Zhao & J. You, "Recent progresses on defect passivation towards efficient perovskite solar cells", Adv. Energy Mater **10** (2019) 1902650. https://onlinelibrary.wiley.com/doi/abs/10.1002/aenm.201902650.

[11] S. Amole, O. Adedokun, O. Akinrinola, O. A. Oyekanmi, F. A. Ojeniyi, A. K. Dauda & A. O. Awodugba, "Influence of post thermal treatment on characteristics of polycrystalline hybrid perovskite nanoparticle thin films", Sustainable Energy Research **11** (2024) 30. https://doi.org/10.1186//540807-24-00124-0.

[12] M. Fahrul, R. Hanifah, J. Jaafar, M. Aziz, A. Fauzi, M. A. Rahman & M. H. Dzarfan, "Synthesis of graphene oxide nanosheets via modified Hummers' method and its physicochemical properties", Journal Teknologi (Sciences & Engineering) **1** (2015) 189. https://journals.utm.my/jurnalteknologi/article/view/3555.

[13] D. Markus, I. Istiqomah, A. F. Yusril, N. Nasikhudin, A. Yatimah & M. Worawat, "Potential of enhancing rGO based composite and numerous morphological for enhancing supercapacitors performance", Journal of Material Sciences **20** (2023) 2077. https://ceramics.onlinelibrary.wiley.com/doi/full/10.1111/ijac.14377.

[14] A. C. Nkele, U. Uwanko, A. Alshoaibiu, F. I. Ezema, "One-step spin coating of methylammonium lead iodide on SILAR-deposited tin oxide (SnO$_2$) for effective electron transport", Results in Optics **13** (2023) 100521. https://www.sciencedirect.com/science/article/pii/S2666950123001736.

[15] S. Amole, M. Awodele, O. Adedokun, M. Jain & A. O. Awodugba, "Sol-gel spin coating synthesis of TiO$_2$ nanostructure and its optical characterization", Journal of Material Science and Chemical Engineering **7** (2019) 23. http://doi.org/10.4236/msce2019.76003.

[16] A. O. Awodugba & O. Adedokun, "On the physical and optical characterization of CdS thin films deposited by the chemical bath deposition technique", The Pacific Journal of Sci. and Tech **12** (2011) 334. https://www.scirp.org/reference/referencespapers?referenceid=2537712.

[17] O. Adedokun, P. Sivaprakas, A. Ajani, I. T. Bello, S. Arumugam, "Structural, optical and magnetic studies of sol-gel synthesized Mg-doped pure anatase TiO$_2$ nanoparticles for spintronic and optoelectronics applications", Physica B **667** (2023) 415199. https://www.sciencedirect.com/science/article/abs/pii/S0921452623005665.

[18] O. Adedokun, Y. K. Sanusi & A. O. Awodugba, "Pigment extracts of citrus peels as light sensitizers for dye-sensitized solar cells", Journal of Material Sciences and Applications **3** (2017) 1. https://www.academia.edu/104324249/Pigment_Extracts_of_Citrus_Peels_as_Light_Sensitizers_for_Dye_Sensitized_Solar_Cells?uc-sb-sw=111804670.

[19] A. R. M. Yusoff & M.K. Nazeeruddin, "Low-Dimensional perovskites: From synthesis to stability in perovskite solar cells", tAdv. Energy Mater **8** (2018) 1702073. https://onlinelibrary.wiley.com/doi/abs/10.1002/aenm.201702073.

[20] C. H. Chieng, K. Nazeeruddin, M. Gratzelc & C. G. Wu, "The synergistic effect on H_2O and DMF towards stable and 20 % efficiency inverted perovskite solar cells", Energy Environ. Sci. **10** (2017) 808. https://pubs.rsc.org/en/content/articlelanding/2017/ee/c6ee03586h/unauth.

[21] A. C. Nkele, A. C. Nwanya, N. M. Shinde, S. Ezugwu, M. Maaza, J. S. Shaiku & F. I. Ezema, "The use of nickel oxide as a hole transport material in perovskite solar cell centrifugation: achieving a high performance and stable device", International Journal of Energy Research **44** (2020) 9839. https://onlinelibrary.wiley.com/doi/abs/10.1002/er.5563.

[22] N. Masclocene & A. Guaghardi, "Coherent nanotwins and dynamic disorder in caecium lead halide perovskite nanocrystals", ACS Nano **11** (2021) 3819. https://pubs.acs.org/doi/full/10.1021/acsnano.7b00017.

[23] Q. Wang, Q. Dang, T. Li, A. Gruverman & J. Hasung, "Thin insulating tunneling contact for efficient and water-resistant perovskite solar cells", Adv Mater **28** (2024) 6734. https://www.osti.gov/biblio/1342746.

[24] H. S. Bhatti, S. T. Hussain, F. A. Khan & S. Hussain, "Synthesis and induced multiferrroicity of perovskite $PbTiO_3$", Appl. Surf. Sci. **367** (2016) 291. https://www.sciencedirect.com/science/article/abs/pii/S0169433216300137.

[25] C. C. Stoumpos, D. H. Cao, D. J. Clark, J. Young, J.M. Rondinelli, J. Jang, J. T. Hupp & M. G. Kanatzidis, "Ruddlesden–Popper hybrid lead iodide perovskite 2D homologous semiconductors", Chem. Mater **28** (2016) 2852. https://pubs.acs.org/doi/full/10.1021/acs.chemmater.6b00847.

[26] K. Subodh, "Spectroscopy of Organic Compounds", Cosmic rays **10** (2006) 143005. https://www.semanticscholar.org/paper/Spectroscopy-of-Organic-Compounds-Kumar/6a31f4490b53074adb4281bb5578947eb33afcdd

[27] R. D. Chavan, D. Prochovic, B. Buczak, M. M. Tavakoli, P. Yedav, M. Fialkowski & C. K. Hong, "Gold Nanoparticle functionalized with fullerene derivatives as an effective interface layer for improving the efficiency and stability of planar perovskite solar cells", Adv. Mater Interface early view **7** (2020) 2001144. https://onlinelibrary.wiley.com/doi/abs/10.1002/admi.202001144.

[28] R. Ihly, A. M. Dowgiallo, M. Yang, P. Schulz, N. J. Stanton, O. G. Reid, A. J. Ferguson, K. Zhu, J.J. Berry and J. L. Blackburn, "Efficient charge extraction and slow recombination in organic– inorganic perovskites capped with semiconducting single walled carbon nanotubes", Energy Environ. Sci. **9** (2016) 1439. https://pubs.rsc.org/en/content/articlelanding/2016/ee/c5ee03806e/unauth.

[29] C. C. Stoumpos, D. H. Cao, D. J. Clark, J. Young, J. M. Rondinelli, J. Jang, J. T. Hupp & M. G. Kanatzidis, "Ruddlesden–Popper hybrid lead iodide perovskite 2D homologous semiconductors", Chem. Mater **28** (2016) 2852. https://pubs.acs.org/doi/full/10.1021/acs.chemmater.6b00847.

[30] M. G. Ju, J. Dai, L. Ma, Y. Zhou & X. C. Zen, "Zero-dimensional organic–inorganic perovskite variant: transition between molecular and solid crystal", J. Am. Chem. **140** (2018) 10456 https://pubs.acs.org/doi/abs/10.1021/jacs.8b03917.